Early winter barium excess in the Southern Indian Ocean as an annual remineralisation proxy (GEOTRACES GIPr07 cruise)

Natasha René van Horsten[1,2,3], Hélène Planquette[1], Géraldine Sarthou[1], Thomas James Ryan-Keogh[2], Nolwenn Lemaitre[5], Thato Nicholas Mtshali[4], Alakendra Roychoudhury[3], and Eva Bucciarelli[1]

[1]Univ Brest, CNRS, IRD, Ifremer, LEMAR, F-29280 Plouzane, France.
[2]SOCCO, CSIR, Lower Hope Road, Cape Town, South Africa, 7700.
[3]TracEx, Department of Earth Sciences, Stellenbosch University, Stellenbosch, South Africa, 7600.
[4]Department of Forestry, Fisheries and Environment, Oceans and Coast, Foretrust Building, Martin Hammerschlag Way, Cape Town, South Africa, 8001.
[5]Department of Earth Sciences, Institute of Geochemistry and Petrology, ETH Zurich, Zurich, Switzerland.

Correspondence to: Natasha van Horsten (natasha.vanhorsten@uct.ac.za), Eva Bucciarelli (Eva.Bucciarelli@univ-brest.fr)

Abstract. The Southern Ocean (SO) is of global importance to the carbon cycle, and processes such as mesopelagic remineralisation that impact the efficiency of the biological carbon pump in this region need to be better constrained. During this study early austral winter barium excess (Ba_{xs}) concentrations were measured for the first time, along 30°E in the Southern Indian Ocean. Winter Ba_{xs} concentrations of 59 to 684 pmol L^{-1} were comparable to those observed throughout other seasons. The expected decline of the mesopelagic Ba_{xs} signal to background values during winter was not observed, supporting the hypothesis that this remineralisation proxy likely has a longer timescale than previously reported. A compilation of available SO mesopelagic Ba_{xs} data, including data from this study, shows an accumulation rate of ~ 0.9 µmol m^{-2} d^{-1} from September to July that correlates with temporally integrated remotely sensed primary productivity (PP), throughout the SO from data spanning ~ 20 years, advocating for a possible annual timescale of this proxy. The percentage of mesopelagic particulate organic carbon (POC) remineralisation as calculated from estimated POC remineralisation fluxes over integrated remotely sensed PP was ~ 2 fold higher south of the polar front (19 ± 15 %, n = 39) than north of the polar front (10 ± 10 %, n = 29), revealing the higher surface carbon export efficiency further south. By linking integrated remotely sensed PP to mesopelagic Ba_{xs} stock we could obtain better estimates of carbon export and remineralisation signals within the SO on annual and basin scales.

1 Introduction

The Southern Ocean (SO) is a carbon sink of global significance responsible for 40 – 50 % of the global oceans' carbon uptake (Friedlingstein et al., 2019; Gregor et al., 2019; Gruber et al., 2019). Oceanic carbon uptake is regulated by various processes, including the biological carbon pump (BCP). Inorganic carbon is consumed and released by photosynthetic organisms through

photosynthesis and respiration (Sarmiento and Gruber, 2006), thereby regulating the earth's carbon cycle by partially sequestering photosynthetically fixed CO_2 in the ocean interior (Honjo et al., 2014). In particular, the SO BCP is a crucial contributor to the earth's carbon cycle by exporting, from surface waters, ~ 3 Pg C yr^{-1} of the ~ 10 Pg C yr^{-1} global export production (Schlitzer, 2002). The efficiency of the BCP is linked to the export and preservation of surface particulate matter and is directly linked to atmospheric CO_2 levels, on glacial-interglacial timescales (Honjo et al., 2014; Sigman et al., 2010). Sedimentation out of the surface layer (~100 m) is defined as surface export and out of the mesopelagic zone (~1000 m) as deep export (Passow and Carlow, 2012). There are large gaps in our knowledge with regard to deep carbon export, internal cycling and the seasonality of these processes (Takahashi et al., 2012). The magnitude of deep carbon export is dependent on the efficiency of mesopelagic remineralisation (Jacquet et al., 2015) which can balance or even exceed particulate organic carbon (POC) surface export, especially later in the growing season, thereby limiting deep export (Buesseler and Boyd, 2009; Cardinal et al., 2005; Jacquet et al., 2011, 2015; Lemaitre et al., 2018; Planchon et al., 2013). A possible explanation for imbalances between surface export and mesopelagic processes can be lateral advection of surface waters with lower particle export relative to the mesopelagic signal (Planchon et al., 2013). It is also possible that continued remineralisation of earlier larger export fluxes is detected in the mesopelagic signal but not in the export fluxes of in situ observations (Planchon et al., 2013). In addition to this, the efficiency of remineralisation is influenced by the size and composition of exported particles (Rosengard et al., 2015; Twining et al., 2014) as well as the pathway by which these particles are transported downwards (e.g., eddy-subduction, active migration, sinking or mixing) from the surface mixed layer to the mesopelagic zone (Boyd et al., 2019; Le Moigne, 2019), creating an intricate web of processes to disentangle. Mesopelagic remineralisation has also been shown to be influenced by environmental factors, such as temperature, phytoplankton community structure and nutrient availability (Bopp et al., 2013; Buesseler and Boyd, 2009). Indeed, nutrient limitation in surface waters limits export and consequently mesopelagic remineralisation by promoting the shift to smaller phytoplankton assemblages that preferentially take up recycled nutrients in the surface mixed layer (Planchon et al., 2013). Phytoplankton community composition exerts an important control where diatoms are more efficiently exported, due to their large size and ballasting by biogenic silica, compared to smaller non-diatom phytoplankton (Armstrong et al., 2009; Buesseler, 1998; Ducklow et al., 2001). Latitudinal trends in remineralisation efficiency can also be linked to temperature-dependent heterotrophs that are responsible for remineralisation (DeVries and Weber, 2017; Marsay et al., 2015). The mesopelagic layer is under-studied, especially in the high latitudes, and therefore these processes are poorly constrained, despite their importance to global elemental cycles, including that of carbon (Le Moigne, 2019; Robinson et al., 2010).

Export and remineralisation tracers, such as ^{234}Th/^{238}U and apparent oxygen utilisation (AOU), have been used to study mesopelagic POC remineralisation fluxes (Buesseler et al., 2005; Planchon et al., 2013; Lemaitre et al., 2018). Surface export is set by the deficit of ^{234}Th activities over ^{238}U activities, while remineralisation processes are reflected by ^{234}Th/^{238}U ratios larger than 1 below the surface mixed layer integrating processes over a 2 to 3 week period (Buesseler et al., 2005; Planchon et al., 2013). AOU is the depletion of oxygen (O_2) in the ocean interior relative to surface saturation, due to biological respiration, when surface water masses are subducted. AOU is dependent on salinity and temperature and integrates

64   remineralisation on timescales of years to decades (Ito et al., 2004). Inaccuracies have, however, been detected with AOU as

65   a remineralisation proxy, specifically in high latitude areas, due to O_2 undersaturation as a consequence of large temperature

66   gradients (Ito et al., 2004).

67   Barium excess (Ba_{xs}) is another proxy utilised to yield estimates of mesopelagic POC remineralisation fluxes. It is defined as

68   the "biogenic" portion of particulate barium (pBa) as barite crystals, formed by the decay of bio-aggregates below the surface

69   mixed layer (Bishop, 1988; Dehairs et al., 1980; Lam and Bishop, 2007; Legeleux and Reyss, 1996; van Beek et al., 2007). As

70   these crystals are released, a Ba_{xs} peak is formed within the mesopelagic zone which has been found to correlate to primary

71   production (PP), O_2 consumption and POC remineralisation (Dehairs and Goeyens, 1996; Dehairs et al., 1997). Depth-

72   integrated rates of O_2 consumption between the base of the mixed layer and 1000 m were estimated using an inverse 1-D

73   advection-diffusion-consumption model (Shopova et al., 1995) to develop transfer functions between the Ba_{xs} signal and the

74   rate of surface POC export for subsequent mesopelagic remineralisation (Dehairs and Goeyens, 1996; Dehairs et al., 1997).

75   Strong correlations have been obtained between the well-established export/remineralisation flux proxy [234]Th and Ba_{xs}, during

76   studies conducted in the SO and the North Atlantic, confirming the validity of Ba_{xs} as a remineralisation proxy (Cardinal et

77   al., 2005; Lemaitre et al., 2018; Planchon et al., 2013). Estimates of POC remineralisation fluxes, using the Ba_{xs} proxy, are

78   directly influenced by the background signal of Ba_{xs}, after partial dissolution and sedimentation from the previous bloom

79   season. It can be thought of as "pre-formed" Ba_{xs}, defined as the $Ba_{residual}$ signal at zero O_2 consumption (Jacquet et al., 2015).

80   Because studies conducted in spring and summer suggest that the mesopelagic Ba_{xs} signal lasts between a few days to a few

81   weeks (Dehairs et al., 1997; Cardinal et al., 2005; Jacquet et al., 2007, 2008a), it is postulated that winter measurements should

82   give the true SO $Ba_{residual}$ value (Jacquet et al., 2008b, 2011). In this context, as part of a GEOTRACES process study (GIpr07)

83   of a transect along 30°E in the Southern Indian Ocean (58.5°S to 41.0°S), we studied Ba_{xs} distributions during early austral

84   winter (July 2017) to better constrain the SO $Ba_{residual}$ concentrations and the timescale of this proxy. To our knowledge these

85   are the first reported wintertime values for this proxy in the SO.

86   ## 2   Materials and Methods

87   ### 2.1   Sampling and hydrography

88   During the GEOTRACES GIpr07 cruise, which took place in early austral winter (28 June - 13 July 2017) onboard the R/V

89   *SA Agulhas II*, seven stations were sampled along 30°E, from 58.5°S to 41.0°S (WOCE I06S, Figure 1a). At each station

90   between 15 and 21 samples were collected from 25 m down to 1500 m, for shallow stations, and down to 4250 m, for deep

91   stations, to be analysed for multiple parameters.

92   Positions of the fronts during the cruise were determined using the July monthly mean absolute dynamic topography data from

93   the CLS/AVISO product (Rio et al., 2011), with boundary definitions from Swart et al. (2010). From north to south the

94   identified fronts are, the Subtropical Front (STF), the Subantarctic Front (SAF), the Polar Front (PF), the Southern Antarctic

95   Circumpolar Current Front (SACCf) and the Southern Boundary (SBdy) (Figure 1a). The marginal ice zone, identified as the

position of 30 % ice cover, was positioned at 61.7°S, approximately 3° (356 km) south of the southernmost station (de Jong et

97 al., 2018). Therefore, a potential sea ice influence on our study area can be disregarded.
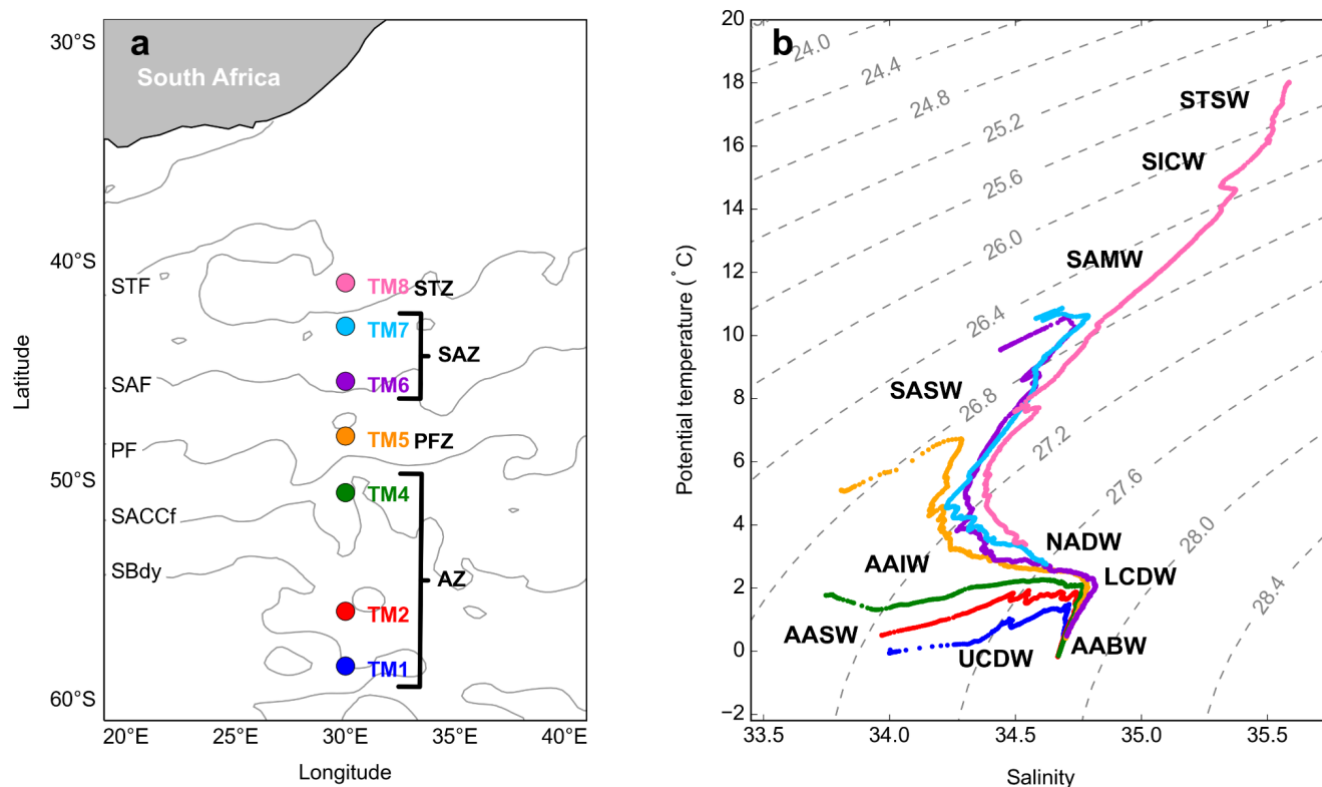
98
99 **Figure 1: (a) GEOTRACES GIPr07 cruise sampling stations overlaid on a map with frontal positions; namely, the Subtropical Front**
100 **(STF), the Subantarctic Front (SAF), the Polar Front (PF), the Southern Antarctic Circumpolar Current Front (SACCf) and the**
101 **Southern Boundary (SBdy), as determined by mean absolute dynamic topography (MADT) and crossing over four zones; namely,**
102 **the Antarctic zone (AZ), the Polar frontal zone (PFZ), the Subantarctic zone (SAZ) and the Subtropical zone (STZ). (b) Potential**
103 **temperature plotted against salinity, overlaid on isopycnals and identification of water masses sampled; namely, Subtropical Surface**
104 **Water (STSW), South Indian Central Water (SICW), Subantarctic Mode Water (SAMW), Subantarctic Surface Water (SASW),**
105 **Antarctic Intermediate Water (AAIW), Antarctic Surface Water (AASW), North Atlantic Deep Water (NADW), Lower**
106 **Circumpolar Deep Water (LCDW), Upper Circumpolar Deep Water (UCDW), and Antarctic Bottom Water (AABW).**

107 ### 2.2 Temperature, salinity and dissolved O$_2$

108 Temperature (°C), salinity and dissolved O$_2$ (μmol L^{-1}) profiles were measured by sensors (SBE 911plus) which were

109 calibrated by the manufacturer within a year prior to the cruise. At each cast, discrete seawater samples were collected and

110 analysed onboard for in situ calibration of sensor data for salinity (8410A Portasal salinometer, $R^2 = 0.99$) and dissolved O$_2$

111 concentrations (Metrohm 848 titrino plus, $R^2 = 0.83$; Ehrhardt et al., 1983). Temperature and salinity measurements were used

112 to calculate potential density (σ_θ; Gill, 1982) to characterise water masses sampled and to identify the mixed layer depth

113 (MLD). The MLD is the depth at which there is a change of 0.03 kg m^{-3} in σ_θ from a near-surface value at ~ 10 m (de Boyer

114 Montégut, et al., 2004). Decreases in dissolved O$_2$ concentrations at intermediate depths, together with Ba$_{xs}$ concentrations,

115 were used to define the mesopelagic remineralisation layer.

2.3   pBa and particulate aluminium

Profile sampling of the water column was conducted with a GEOTRACES compliant trace metal clean CTD housed on an epoxy coated aluminium frame with titanium bolts equipped with 24 x 12 L trace metal clean Teflon coated GO-FLO bottles (General Oceanics). All sampling and analyses were conducted following the GEOTRACES clean sampling and analysis protocols (Cutter et al., 2017). Volumes of 2 to 7 L seawater were filtered from the GO-FLO bottles onto acid-washed polyethersulfone filters (25 mm diameter, Supor, 0.45 µm pore size), for pBa and particulate aluminium (pAl) analyses. Filters were mounted in-line on the side spigot of each Go-Flo bottle, on swinnex filter holders. Furthermore, bottles were mixed 3 times before filtration, as recommended by the GEOTRACES protocols (Cutter et al., 2017), to ensure homogenous sampling. Although the large fast-sinking fraction of particles may be under-sampled by using bottles (Bishop and Edmond, 1976; Planquette and Sherrell, 2012), comparing data that were generated using the same, internationally validated sampling systems and protocols (Cutter et al. 2017), as we do in this study, minimises potential bias. After filtration, filters were placed in trace metal clean petri slides (Pall) and kept frozen at -20°C until further processing on land. Sample processing was conducted under a class 100 HEPA filtered laminar flow and extraction hood in a clean laboratory.

The pBa and pAl samples were processed and analysed 6 months after sample collection, at LEMAR (France). Unused blank filters and filters containing the samples were acid reflux digested at 130°C in acid-cleaned savillex vials using a mixture of HF and HNO_3 (both Ultrapure grade, Merck) solutions (Planquette and Sherrell, 2012). Archive solutions were stored in 3 ml of 0.12 M HNO_3 (Ultrapur grade), of which 250 µL was diluted up to 2 mL for analysis by sector field inductively coupled plasma mass spectrometry (SF-ICP-MS, Element XR Thermo Scientific). Samples were spiked with 1 µg L^{-1} indium as an internal standard to correct for instrument drift. The detection limits, defined as three times the standard deviation of the blanks (unused filter blanks), were 0.39 pmol L^{-1} and 0.03 nmol L^{-1} (n = 5) for pBa and pAl, respectively. Mean amounts (in nmol) of a given element determined in unused filter blanks were subtracted from the amounts in the sample filter then divided by the volume filtered. Three certified reference materials (BCR 414, MESS 4 and PACS 3) were processed and analysed with the samples to assess the accuracy of the methodology. Our values were in good agreement with the certified values of the reference materials (Table 1) (Jochum et al., 2005). Percentage error of analyses was determined by the repeat analysis of random samples during each run, the mean percentage error of sample analysis for pBa and pAl was 9.2 ± 2.5 % and 11.1 ± 4.6 % (mean ± SD, n = 6), respectively.

Table 1: Certified reference material recovery data for accuracy determination of pBa and pAl analyses
N/A refers to instances where there are no certified values available to check for accuracy

	pBa (mg/kg)	pAl (mg/kg)
PACS 3 certified (mean ± SD)	N/A	65800 ± 1700
PACS 3 measured (mean ± SD)	N/A	73156 ± 15416
PACS 3 mean % recovery	N/A	111 ± 23

MESS 4 certified	920	79000 ± 2000
MESS 4 (mean ± SD)	1033 ± 28	100048 ± 26870
MESS 4 mean % recovery ± SD	112 ± 3	127 ± 34
BCR 414 indicative values	32 ± 5	2384 ± 652
BCR 414 (mean ± SD)	34 ± 4	2651 ± 317
BCR 414 mean % recovery ± SD	105 ± 12	111 ± 13

144

2.4 Ba_{xs} as a proxy for mesopelagic POC remineralisation

The non-lithogenic fraction of pBa, Ba_{xs}, was calculated by subtracting the lithogenic fraction of pBa from the total pBa measured using Eq. 1. The lithogenic contribution to pBa was calculated by multiplying the pAl concentration with the Ba/Al upper continental crust (UCC) ratio, 0.00135, as determined by Taylor and McLennan (1985).

$$Ba_{xs} = [pBa] - ([pAl] \times (Ba/Al)_{UCC}) \tag{1}$$

Total pBa and Ba_{xs} profiles were nearly identical with a mean percentage Ba_{xs} to total pBa of 99 ± 1 % (mean ± SD, n = 124; Table S1), indicating that pBa from lithogenic sources was negligible. This ensures the accurate estimation of Ba_{xs}, which requires that less than 50 % of pBa should be associated with lithogenic inputs (Dymond et al., 1992).
The mesopelagic POC remineralisation flux was estimated using Eq. 2 (Dehairs and Goeyens, 1996; Shopova et al., 1995):

$$Mesopelagic\ POC\ remineralisation = Z \times JO_2 \times (C{:}O_2)_{Redfield\ Ratio} \times 12.01 \tag{2}$$

Where the mesopelagic POC remineralisation flux is expressed in mg C m^{-2} d^{-1}, Z is the depth range of the mesopelagic Ba_{xs} layer (100 - 1000 m), C:O_2 is the stoichiometric molar ratio of carbon to O_2 consumption by remineralisation as per the Redfield Ratio (127/175, Broecker et al., 1985), 12.01 is the molar mass of carbon (g mol^{-1}) and JO_2 is the rate of O_2 consumption (µmol L^{-1} d^{-1}) as estimated using Eq. 3:

$$JO_2 = (Mesopelagic\ Ba_{xs} - Ba_{residual})/17200 \tag{3}$$

Eq. 3 (Dehairs and Goeyens, 1996; Shopova et al., 1995) is the linearisation of the exponential function by Dehairs et al. (1997). Mesopelagic Ba_{xs} is the depth-weighted average Ba_{xs} of the mesopelagic zone (pmol L^{-1}), the constant value of 17200 is the slope of the linear regression of depth-weighted average Ba_{xs} (pmol L^{-1}) versus O_2 consumption rate (µmol L^{-1} d^{-1}) and

169    $Ba_{residual}$ is the deep ocean background value of Ba_{xs} at zero oxygen consumption. The literature value of 180 pmol L^{-1} was

170   used as the $Ba_{residual}$ value (Jacquet et al, 2008a; 2008b; 2011; 2015; Planchon et al., 2013) in our calculations.

171   The integrated mesopelagic Ba_{xs} stock (μmol m^{-2}) over the mesopelagic layer (100 - 1000 m) was calculated from the depth-

172   weighted average Ba_{xs} in order to investigate the link between the accumulated mesopelagic signal and the corresponding

173   integrated remotely sensed primary productivity (PP).

2.5   Integrated remotely sensed PP

175   The integrated remotely sensed PP (mg C m^{-2} d^{-1}) within the surface mixed layer was calculated using the CbPM algorithm

176   (Behrenfeld et al., 2005), which requires chlorophyll concentration (mg m^{-3}), particulate backscatter (λ 443 nm, m^{-1}),

177   photosynthetically active radiation (PAR; μmol photons m^{-2} d^{-1}) and the MLD (m). Ocean Colour-Climate Change Initiative

178   (OC-CCI) data (https://esa-oceancolour-cci.org/), which blends existing data streams into a coherent record, meeting the

179   quality requirements for climate assessment (Sathyendranath et al., 2019), were used for chlorophyll and particulate

180   backscatter. PAR was taken from GLOB colour (http://www.globcolour.info/), and the MLD was taken from the climatology

181   of de Boyer Montegut et al. (2004). The integrated remotely sensed PP data were regridded to 0.25° spatially, using bilinear

182   interpolation using the Python programming package xESMF (Zhuang, 2018), and averaged monthly. The area-averaged PP

183   was averaged over a 6 x 1° rectangular sample area, positioned 6° upstream longitudinally, and 1° latitudinally centred around

184   each sampled station (see discussion for details). In order to assess the validity of the remotely sensed PP data and demonstrate

185   no meridional bias across the SO, the percentage valid pixels was calculated for data north (90 ± 20 %; mean ± SD, n = 370)

186   and south (82 ± 29 % mean ± SD, n = 488) of the PF, revealing no bias.

2.6   Integrated % POC remineralised

188   The integrated remineralised POC (mg C m^{-2}) was estimated by multiplying the POC remineralisation flux (mg C m^{-2} d^{-1}), as

189   estimated using the Ba_{xs} proxy method, by the number of days over which the corresponding remotely sensed PP (mg C m^{-2} d^{-1})

190   was subsampled. The % POC remineralised was then estimated as the percentage of integrated remotely sensed PP (mg C

191   m^{-2}) remineralised, assuming that the mesopelagic Ba_{xs} stock signal observed is due to the remineralisation of the integrated

192   surface PP signal.

2.7   Statistical analysis

194   For statistical analysis, the least squares regression method was applied for assessment of significant correlations (Barbur et

195   al., 1994). Significant differences between regions and regressions were tested using Welch's t-test, with an alpha of 0.05 (95

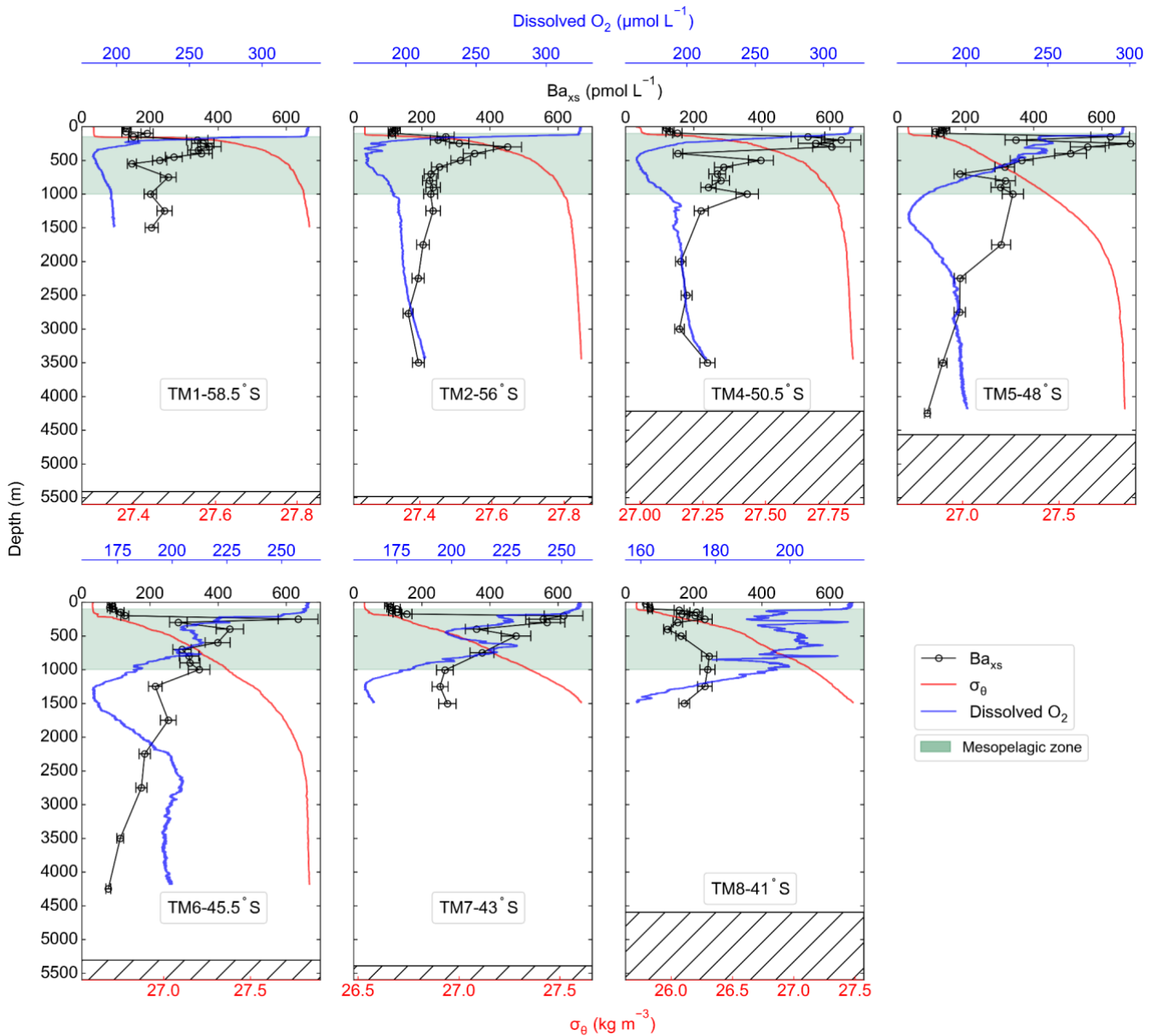196   % confidence level) (Kokoska and Zwillinger, 2000).

3 Results

3.1 Hydrography

The potential temperature (θ) and salinity (S) along the transect ranged from -0.06 to 18.03 °C and from 33.77 to 35.59, respectively. Where surface θ and S define four hydrographic zones; namely, the Antarctic zone (AZ; $\theta < 2.5$ °C; $S \leq 34$) from ~ 50°S to 58.5°S, the polar frontal zone (PFZ; $\theta \cong 5$ °C; $S \cong 33.8$) at ~ 48°S, the subantarctic zone (SAZ; $5 < \theta < 11$ °C; $33.8 < S < 34.7$) between 43°S and 45.5°S, and the subtropical zone (STZ; $\theta \geq 17.9$ °C; $S \cong 35.6$) at 41°S (Figure 1a; Anilkumar and Sabu, 2017; Orsi et al., 1995; Pollard et al., 2002). The MLDs along the transect ranged between 97 and 215 m (144 ± 39 m; mean $\pm$ SD, n = 7), shoaling towards the PF (Table S2).

As can be observed on the T-S plot of stations sampled (Figure 1b), different water masses were sampled along the transect throughout the water column. South of the polar front (SPF; $\gtrsim$ 50°S; TM1, 2 and 4), from surface to depth, Antarctic Surface Water (AASW; $27 < \sigma_\theta < 27.4$ kg.m^{-3}), Upper and Lower Circumpolar Deep Water (UCDW; $27.2 < \sigma_\theta < 27.75$ kg.m^{-3} and LCDW; $27.75 < \sigma_\theta < 27.85$ kg.m^{-3}, respectively), and Antarctic Bottom Water (AABW; $27.8 < \sigma_\theta < 27.85$ kg.m^{-3}) were characterised. North of the polar front (NPF) and south of the STF (< 50°S; TM5, 6 and 7), from surface to depth, Subantarctic Surface Water (SASW; $26.5 < \sigma_\theta < 26.75$ kg.m^{-3}), Antarctic Intermediate Water (AAIW; $26.7 < \sigma_\theta < 27.4$ kg.m^{-3}), North Atlantic Deep Water (NADW; $27 < \sigma_\theta < 27.85$ kg.m^{-3}) and, as far north as 45.5°S, AABW close to the ocean floor, were identified. At the northernmost station (TM8; 41°S), in the STZ, the water masses sampled include Subtropical Surface Water (STSW; $\sigma_\theta \cong 25.7$ kg.m^{-3}), South Indian Central Water (SICW; $25.8 < \sigma_\theta < 26.2$ kg.m^{-3}), Subantarctic Mode Water (SAMW; $26.2 < \sigma_\theta < 26.6$ kg.m^{-3}), AAIW and NADW.

3.2 Dissolved O$_2$

The water column dissolved O$_2$ concentrations ranged from 159 to 333 µmol L^{-1} (Figure 2). Maximum concentrations were observed in the surface mixed layer, increasing southwards along the transect, with a mean value of 287 ± 40 µmol L^{-1} (mean $\pm$ SD, n = 700). A decrease in concentrations below the MLD coincided with an increase in σ_θ. South of the PF, the decrease in dissolved O$_2$ concentrations at the MLD was sharp and relatively shallow when compared to profiles NPF, which were more gradual, spanning a wider depth range. Within the mesopelagic zone concentrations decreased down to 204 ± 29 µmol L^{-1} (mean $\pm$ SD, n = 6373), then remained relatively uniform below 1000 m at 192 ± 113 µmol L^{-1} (mean $\pm$ SD, n = 12950).

226 **3.3 Ba$_{xs}$ and estimated POC remineralisation fluxes**

227 Along the transect, Ba$_{xs}$ concentrations ranged from 59 to 684 pmol L^{-1}. All profiles exhibited a depletion of Ba$_{xs}$ in the upper

228 surface waters (59 - 152 pmol L^{-1}), then a rapid increase below the MLD (~ 150 m), with concentrations ranging between 113

229 and 684 pmol L^{-1} in the mesopelagic zone (100 - 1000 m, Figure 2). At the two southernmost stations (TM1 and TM2),

9

230   mesopelagic Ba_{xs} peaks spanned a narrower depth range (100 - 600 m) than stations further north, with concentrations reaching

231   values of ~ 400 pmol L^{-1}. Concentrations were higher in the PFZ and SAZ with a maximum of 684 pmol L^{-1} in the PFZ, at

232   48°S (TM5). The subsurface increase of Ba_{xs} started at slightly deeper depths (150 - 200 m) and spanned wider depth ranges

233   down to 1000 m, at stations north of the PF. The STZ station, at 41°S (TM8), had the lowest concentrations, only increasing

234   up to ~ 200 pmol L^{-1}. Double peaks were observed at all stations north of the PF, with a shallow and more substantial peak

235   occurring in the upper mesopelagic zone and a second peak in the lower mesopelagic zone. Below the mesopelagic zone, Ba_{xs}

236   concentrations decreased down to ~ 180 pmol L^{-1} and remained relatively uniform.

237   The mean $Ba_{residual}$ concentration south of the PF was 183 ± 29 pmol L^{-1} (mean $\pm$ SD, n = 7), whereas it was 142 ± 45 pmol L^{-1}

238   (mean $\pm$ SD, n = 8) between the PF and the STF. The two regions were however not significantly different to each other

239   when conducting a Welch's t-test (t-statistic = 2.10; p-value = 0.06) and when averaging all concentrations below 2000 m

240   along the transect, the $Ba_{residual}$ concentration was 161 ± 43 pmol L^{-1} (mean $\pm$ SD, n = 15). This concentration is not statistically

241   different from the literature value of 180 pmol L^{-1} (Jacquet et al, 2008a; 2008b; 2011; 2015; Planchon et al., 2013), which is

242   widely used for estimates of POC remineralisation fluxes. For a better comparison with these previous estimates, we used 180

243   pmol L^{-1} for the $Ba_{residual}$ concentration in our calculations.

244   The estimated POC remineralisation fluxes for the study area ranged from 6 to 96 mg C m^{-2} d^{-1} (Table S3), increasing

245   northwards from the southernmost station up to the PFZ from 32 to 92 mg C m^{-2} d^{-1}, then decreasing down to 70 mg C m^{-2} d^{-1}

246   at the SAF. The highest flux was estimated in the SAZ, and the lowest flux was estimated in the STZ.

247   **4   Discussion**

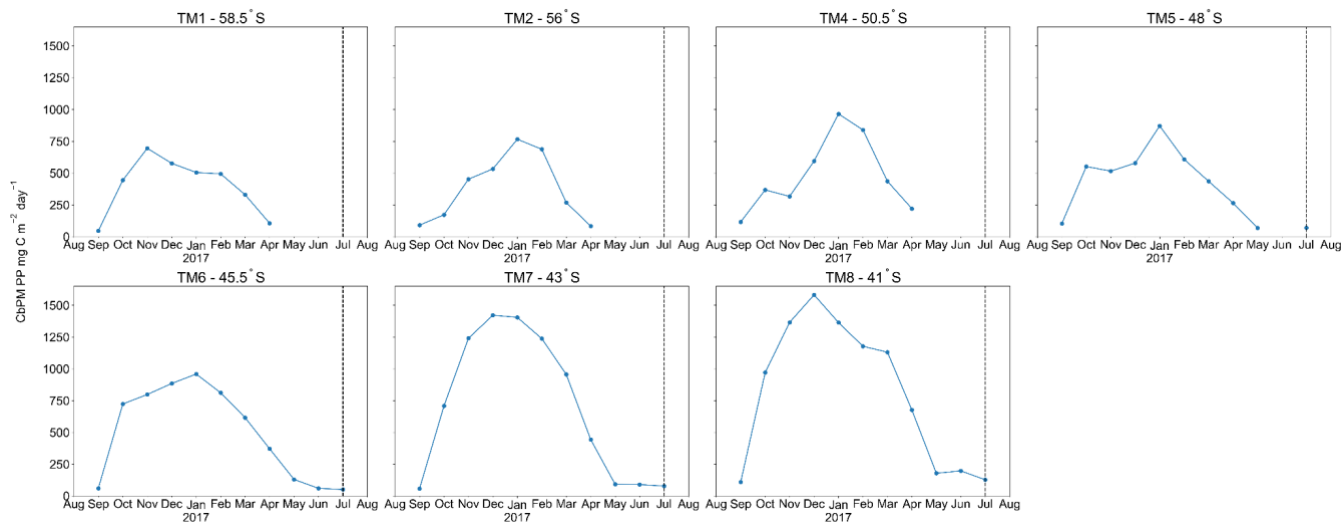248   **4.1   Early wintertime Ba_{xs} and $Ba_{residual}$ concentrations**

249   A noticeable difference between profiles sampled early in the bloom season (Dehairs et al., 1997; Jacquet et al., 2015) versus

250   those sampled later (Cardinal et al., 2001; Planchon et al., 2013) is the contrasted Ba_{xs} concentrations in the surface mixed

251   layer. Dehairs et al. (1997) has shown that these concentrations of Ba_{xs} can be as high as 9000 pmol L^{-1} in areas of high

252   productivity during spring, which then become depleted to concentrations below the SO $Ba_{residual}$ value of ~ 180 pmol L^{-1}, as

253   productivity declines and surface POC export increases (Planchon et al., 2013). These high surface concentrations are,

254   however, not due to the same process as the one that controls the Ba_{xs} concentrations within the mesopelagic zone (Jacquet et

255   al., 2011). Surface water concentrations are associated with Ba adsorbed onto particles whereas the mesopelagic Ba_{xs} signal is

256   due to barite crystals formed within decaying bio-aggregates (Cardinal et al., 2005; Lam and Bishop, 2007; Lemaitre et al.,

257   2018; Sternberg et al., 2005). In this study, we observed surface depletion of Ba_{xs} at all stations, in line with the assumption

258   that the bulk surface export from the preceding bloom had been achieved at the time of sampling and, the majority of the Ba_{xs}

259   had been transferred to the mesopelagic zone.

260   A sharp increase in σ_{θ} observed at the MLD has previously been identified as the depth at which decaying bio-aggregates are

261   formed (Lam and Bishop, 2007). These increases coincided with an increase in Ba_{xs} (Figure 2), linking the subsurface Ba_{xs}

signal to decaying bio-aggregates as per previous studies (Cardinal et al., 2005; Dehairs et al., 1997; Jacquet et al., 2011). Additionally, decreases observed in dissolved O_2 profiles along the transect were also accompanied by coinciding increases in Ba_{xs}, in line with O_2 consumption due to remineralisation within the mesopelagic zone (Figure 2) (Cardinal et al., 2005; Jacquet et al., 2005, 2011). The observed range of mesopelagic Ba_{xs} concentrations (113 - 684 pmol L^{-1}) were comparable to those previously reported in SO open waters (~ 200 - 1000 pmol L^{-1}; Cardinal et al., 2001, 2005; Jacquet et al., 2005, 2008a, 2008b, 2011, 2015; Planchon et al., 2013).

Ba_{xs} profiles exhibited similar distributions to those reported throughout bloom seasons in the SO, with distinct peaks observed within the mesopelagic zone at all stations. Earlier in the bloom season, peaks mostly occur within the upper half of the mesopelagic zone (100 - 500 m: Cardinal et al., 2001, 2005; Jacquet et al., 2005, 2008a, 2011, 2015), but as the season progresses, they deepen down towards the bottom half of the mesopelagic zone (500 - >1000 m: Jacquet et al., 2008b, Planchon et al., 2013). Deepening and widening of the remineralisation depth range can be expected as the season progresses, due to continued remineralisation taking place as particles sink to the bottom of the mesopelagic zone (Lemaitre et al., 2018; Planchon et al., 2013). This is also what we observed during early winter at stations NPF, with a second peak in deeper waters, as observed by Jacquet et al. (2008b) during the iron (Fe) fertilisation experiment (EIFEX). The deeper peak could also be linked to relatively larger cells that sink faster as they remineralise, possibly a large bloom earlier in the season.

A distinct latitudinal trend in mesopelagic depth-weighted average Ba_{xs} has generally been observed in the SO with the highest values in the PFZ, decreasing north and southwards from the PF. These latitudinal trends tend to be accompanied by a coinciding trend in in situ surface biomass measurements (Cardinal et al., 2005; Dehairs et al., 1997, Jacquet et al., 2011; Planchon et al., 2013). During our early winter study, we observed a similar latitudinal trend in mesopelagic Ba_{xs} stock (μmol m^{-2}), with an increase from the southernmost station up to the PF, then varying around a maximum in the SAZ, down to the lowest value in the STZ, whereas temporally integrated remotely sensed PP increased progressively northwards to a maximum in the STZ (Figure S1). Time of sampling and extended blooms, which are characteristic of the SAZ (Thomalla et al., 2011), could be contributing factors to the higher values observed in PP and mesopelagic Ba_{xs} distributions at stations north of the PF (Figure S1). Contrary to what was expected, the profiles observed during our early winter study still show a significant mesopelagic remineralisation signal, well after the summer bloom termination, which occurred between April and May (Figure 3), as defined by the point in time when community losses outweigh the growth rate (Thomalla et al., 2011).

292   In deeper waters (below 2000 m) along the transect, south of the STF, where remineralisation is minimal compared to the

293   mesopelagic zone, our Ba$_{xs}$ concentrations of 161 ± 43 pmol L^{-1} (mean ± SD, n = 15) is not significantly different from the

294   widely used Ba$_{residual}$ concentration of 180 pmol L^{-1}, measured during early Spring to late Summer (e.g., Jacquet et al., 2008a;

295   2008b; 2011; 2015; Planchon et al., 2013). We thus did not observe a wintertime decline to an expected "true" SO background

296   value, when PP and bacterial activity are suspected to be minimal (Jacquet et al., 2011). There are two possible explanations

297   for this; firstly, the decline to a winter background signal might never be achieved due to ongoing barite precipitation and

298   remineralisation, as well as the release of labile Ba attached to phytoplankton as they decay, precipitating into barite crystals,

299   which could possibly continue throughout winter (Cardinal et al., 2005). Secondly, the low sinking speed of suspended barite

300   (~ 0.3 m d^{-1}, Sternberg et al., 2008), once produced in the mesopelagic layer, implies that it would take ~ 6 years (not

301   considering reaggregation and redissolution) to sink from 300 m (~ peak of production) to the bottom of the mesopelagic layer

302   (1000 m). The "true" background value may thus have to be measured at the very end of winter just before the initiation of the

303   spring bloom. This also suggests that the Ba$_{xs}$ signal in the mesopelagic layer may represent remineralisation activity over

304   more than a few days to weeks, per previous reports (e.g., Dehairs et al., 1997; Jacquet et al., 2015; Planchon et al., 2013).

305   **4.2   Timescale of the mesopelagic Ba$_{xs}$ signal**

306   The Ba$_{xs}$ signal that we observed in winter is in agreement with the suggestion by Dehairs et al. (1997), that there can be

307   significant carry over between bloom seasons. Other studies have also pointed out that the timescale of this proxy is longer

308   than a snapshot view (Cardinal et al., 2005) and have highlighted a seasonal increase in mesopelagic Ba$_{xs}$ (Jacquet et al., 2011).

309   This strongly suggests that the Ba$_{xs}$ signal is not directly linked to synoptic measurements of PP at the time of sampling. In

310   order to investigate this hypothesis, for the first time, we compiled a SO mesopelagic Ba$_{xs}$ stock dataset with all available

literature data including data from this study (Figure 4a, Table S3). The mesopelagic Ba_{xs} stock was integrated over the Ba_{xs} peak depth range (as identified in each study). As can be seen on the map of the compilation dataset (Figure 4a), these data points were collected across the three basins of the SO, over ~ 20 years. Despite this diversity in observations, a statistically significant accumulation of mesopelagic Ba_{xs} with time is still observed, SPF (Figures 4b) and NPF (Figures 4c). Mesopelagic Ba_{xs} accumulates at a rate of 0.86 (±0.15) µmol m^{-2} d^{-1} SPF ($R^2 = 0.43$, p-value < 0.05, n = 43; Figure 4b), and at 0.88 (±0.20) µmol m^{-2} d^{-1} NPF ($R^2 = 0.41$, p-value < 0.05, n = 31; Figure 4c), with no statistically significant difference between the two regions (Welch's t-test = 0.24; p-value = 0.80).

A possible link between the integrated mesopelagic Ba_{xs} stock and the corresponding integrated remotely sensed PP was assessed for all studies conducted after September 1997, when remotely sensed PP data became available. To do so, we first estimated that sub millimetre sized aggregates would take ~ 20 days to sink down to 1000 m (considered as the bottom of the mesopelagic zone in this study), using a sinking speed of 50 m d^{-1}, that corresponds to an average literature value (50 - 100 m d^{-1}: Riebesell et al., 1991; 50 - 430 m d^{-1} around South Georgia: Cavan et al. 2015; mean of ~ 100 m d^{-1} in the SO as reviewed in Laurenceau-Cornec et al., 2015; Marguerite Bay: 10 - 150 m d^{-1}: McDonnell and Buesseler, 2010). Assuming a maximum surface current speed of 0.2 m s^{-1} (Ferrari and Nikurashin, 2010), it was estimated that these aggregates would have originated, 346 km west from the station that was sampled for mesopelagic Ba_{xs}, ~ 20 days prior. Using this distance, the dimensions of the sample area were set with the southernmost station (TM1) of this study, where degrees of longitude cover the smallest area. For the sake of consistency this sample area was applied to all sampling locations of the considered dataset. The integrated remotely sensed PP (see section 2.5) was then averaged spatially, positioned 6° upstream longitudinally, and 1° latitudinally centred around each station, in order to capture the surface PP that is assumed to translate to the mesopelagic remineralisation and measured Ba_{xs} stock.

The monthly averaged remotely sensed PP, at the time of sampling, was compiled for the considered dataset, and we found that the PP over the growing season (Figure 4d & e) reaches highest values between January and February (day 125 to 175 of the year), thereafter, steadily decreasing to minimal values in July (~ day 310 of the year, i.e., during our study). The mesopelagic Ba_{xs} accumulation over time can, therefore, not be matched with the remotely sensed PP measured during the month of sampling. A possible relationship between mesopelagic Ba_{xs} stock and temporally integrated remotely sensed PP was further investigated by considering longer timescales. Remotely sensed PP of the preceding bloom was temporally integrated from the preceding September, prior to sampling, as the start of the bloom, in general agreement with previous bloom phenology studies (Thomalla et al., 2011), up to one month prior to the sampling date of the study, taking into consideration time needed for export, aggregate formation and barite crystal release through remineralisation (~ 1 month).

13

340
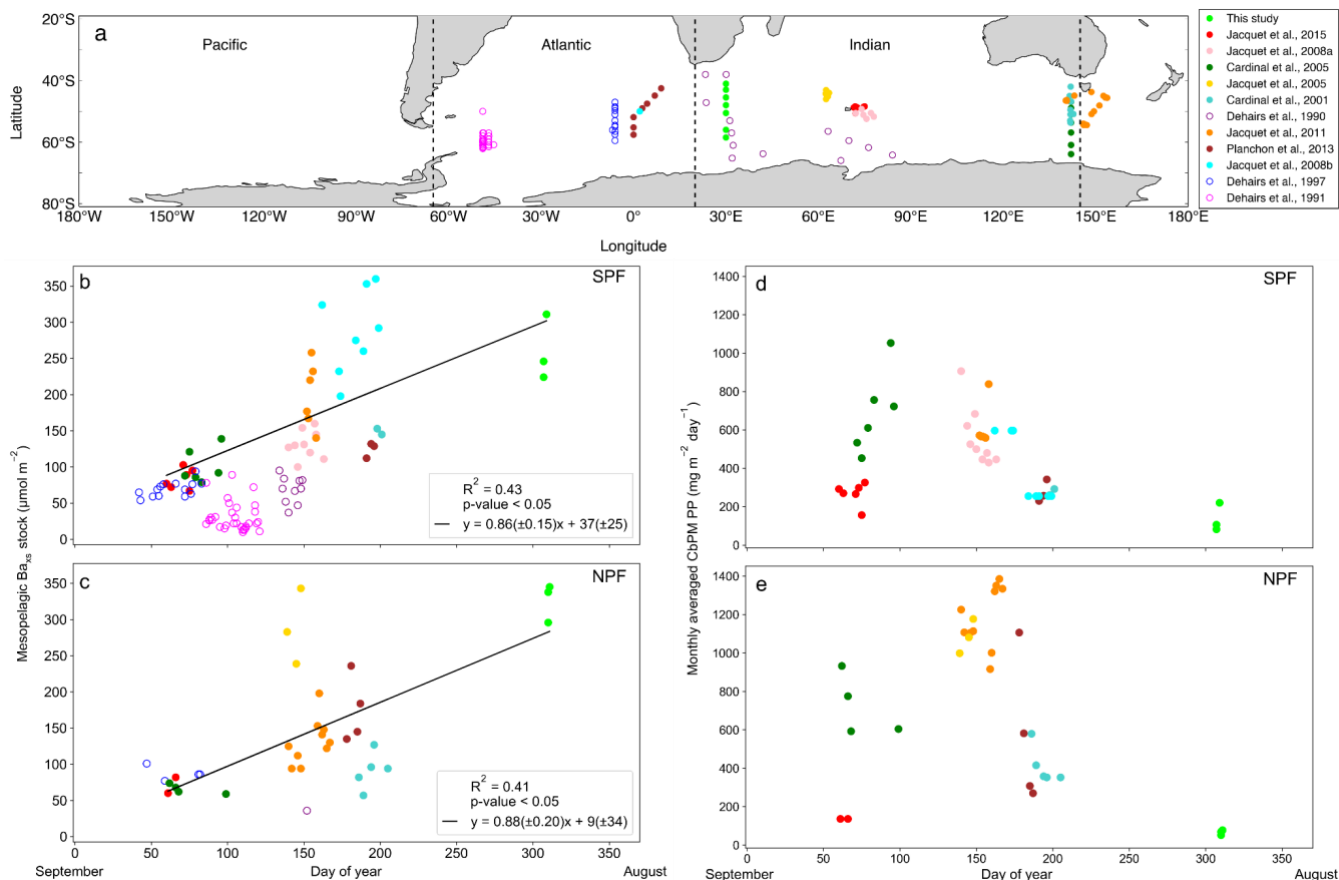
Figure 4: (a) Positions of Ba$_{xs}$ observations compiled from all known SO studies, on a cylindrical equal-area projection of the SO, the three SO basin cut offs are indicated by the dashed black lines, from left to right, Pacific, Atlantic and Indian. Integrated mesopelagic Ba$_{xs}$ stock plotted against day of year sampled, with the 1st of September set as day 1, for all available literature data and winter data from this study. Data was split into two zones using the Polar Front (PF) to divide the SO; (b) South of the PF (SPF) and (c) North of the PF (NPF). Monthly averaged remotely sensed PP plotted against day of year, for locations and dates of the SO compilation dataset and winter data from this study; (d) SPF and (e) NPF. Open circles are data points from studies which did not use HF in the particulate sample digestion procedure, regressions did not include these data, there was, however, no significant difference when including these data points (Table S3).

349   Varying timescales were considered between the preceding September up to 1 month prior to sampling (Sept - T1; Table S4),

350   in monthly increments, that could influence the relationship between remotely sensed PP and the mesopelagic Ba$_{xs}$ stock (Table

351   S4). The strongest and most significant correlation between the mesopelagic Ba$_{xs}$ stock and integrated remotely sensed PP, for

352   both north and south of the PF, was obtained from the preceding September up to 1 month prior to sampling (Table S4, Sept -

353   T1, SPF: Figure 5a, $R^2 = 0.55$, p-value < 0.05, n $= 39$; NPF: Figure 5b, $R^2 = 0.42$, p-value < 0.05, n $= 31$). When remote sensing

354   data was limited due to cloud cover and low sunlight during winter months, specifically at the southernmost stations, all

355   available data was used for the duration of the season. The correlation observed in the STZ is not significant at a 95 %

356   confidence level (p-value $= 0.10$); however, the limited number of data points (n $= 6$) may preclude any significance from

14

emerging. The significant positive correlations obtained south of the STF suggest that mesopelagic Ba_{xs} stock can be used as a remineralisation proxy on an annual timescale instead of only a few weeks. Figure 5 also reveals that for a given PP the mesopelagic Ba_{xs} stock was 2-fold higher SPF compared to NPF (Welch's t-test, t-statistic = 2.24; p-value < 0.05), this is further discussed below.
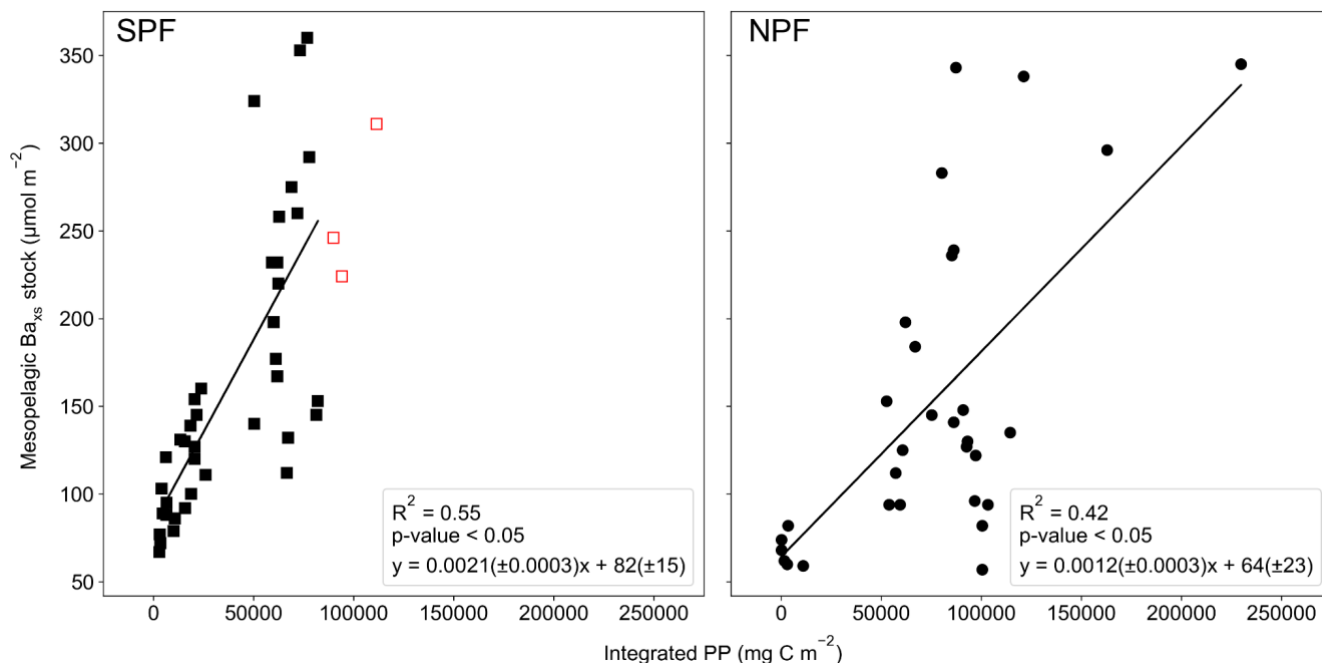
Figure 5: Integrated mesopelagic Ba_{xs} stock plotted against integrated remotely sensed PP from the preceding September up to one month prior to sampling, all available literature data and winter data from this study, (a) South of the PF (SPF, black squares) and (b) North of the PF (NPF, black circles). Red open squares are data points from our winter dataset where there was not sufficient remote sensing PP data to integrate up to 1 month prior to sampling and available data up to 3 months prior to sampling was plotted but not included in the statistical analysis.

4.3 Environmental factors influencing mesopelagic remineralisation and carbon export efficiency

Estimated POC remineralisation fluxes along the transect (6 - 96 mg C m^{-2} d^{-1}) were on the upper end of the range of fluxes reported in previous studies, with the exception of the STZ station, but within the same order of magnitude for the SO as estimated from spring to autumn (0.2 - 118 mg C m^{-2} d^{-1}; Table S3; Cardinal et al., 2005; Jacquet et al., 2011, 2015; Planchon et al., 2013). As the bloom season progresses, more efficient remineralisation rates have been reported in multiple studies (Cardinal et al., 2005; Jacquet et al., 2011; Planchon et al., 2013). However, during late summer as the bloom declines, observations indicate an inefficient BCP due to enhanced surface nutrient recycling (Dehairs et al., 1992; Jacquet et al., 2011; Planchon et al., 2013), leading to a decrease in surface POC export (Planchon et al., 2013). Seasonal variation is reported to be more pronounced northwards within the SO with the least variation observed in the southern Antarctic circumpolar current (Dehairs et al., 1997; Planchon et al., 2013).

The percentage of mesopelagic POC remineralisation as calculated from estimated POC remineralisation fluxes over integrated remotely sensed PP, for the SO compilation dataset (SPF; 19 ± 15 %, n = 39 and NPF; 10 ± 10 %, n = 29; mean $\pm$ SD; t-statistic = 2.75; p-value <0.05; Table S3), was ~ 2 fold higher SPF than NPF, revealing the higher surface carbon export efficiency SPF. Our estimates of % POC remineralised fall within the range of reported export efficiencies throughout the SO (2 - 58 %; Jacquet et al., 2011; Morris et al., 2007; Savoye et al., 2008). Our values also support the inverse relationship between export efficiency and productivity, with higher export efficiency in areas of lower production, High Productivity Low E-ratio (HPLE), where E-ratio refers to the ratio between export production and net primary productivity (Fan et al., 2020; Maiti et al., 2013). Estimated mesopelagic POC remineralisation has been reported to account for a significant fraction of exported carbon in the PFZ and southwards, from 31 to 97 %, from spring to summer, whereas it only accounts for ~ 50% in the SAZ and SAF, during summer (Cardinal et al., 2005). A combination of variables can influence surface export efficiency and the magnitude of the subsequent mesopelagic remineralisation, even more so when considering longer timescales. These variables include physical dynamics and interlinked biogeochemical factors, i.e., bacterial activity, phytoplankton community structure, zooplankton grazing and nutrient availability (Bopp et al., 2013; Buesseler and Boyd, 2009; Cardinal et al., 2005; Jacquet et al., 2008b; Pyle et al., 2018). In previous studies, supply and loss via physical transport has been deemed negligible relative to decay and loss via production, due to minimal advection and diffusion gradients observed on the timescale of days to weeks. These processes were therefore assumed to have minimal impact on the mesopelagic signal (Dehairs et al., 1997; Planchon et al., 2013; Rutgers van der Loeff et al., 2011). It has, however, been observed that features such as mesoscale eddies can have an effect on Ba_{xs} distribution by influencing particle patterns on a broad spatial scale, homogenising mesopelagic remineralisation signals by causing relatively flat profiles or shallower remineralisation peaks (Buesseler et al., 2005; Jacquet et al., 2008b). The region of our winter study is known for being a mesoscale eddy hotspot due to the South-West Indian Ridge (Ansorge et al., 2015). In the STZ, extremely dynamic submesoscale activity due to the Agulhas return current may indeed have significantly influenced the mesopelagic signal, and may help explain the absence of correlation with integrated surface PP. On the contrary, south of the STF, the significant correlations seem to indicate that physical transport variability is not the main process affecting the mesopelagic Ba_{xs} signal, and that biogeochemical factors may be dominant.

The Fe-limited SAZ (Ryan-Keogh et al., 2018) and AZ (Viljoen et al., 2018) have generally mixed and seasonally changing assemblages of pico-, nano- and micro-phytoplankton (Eriksen et al., 2018; Gall et al., 2001). Diatoms tend to dominate in the silicate-rich waters south of the PF (Petrou et al., 2016; Rembauville et al., 2017; Wright et al., 2010), whilst seasonally silicate-limited waters north of the PF, favour smaller phytoplankton groups (Freeman et al., 2018; Nissen et al., 2018; Trull et al., 2018). HPLE regimes are indeed characteristic of large areas of the SAZ, mainly due to surface POC accumulation caused by non-sinking particles, tending towards less efficient export of smaller cells (Fan et al., 2020). Even when large particles are abundant in HPLE surface layers, a complex grazing community may prevent the export of large particles (Dehairs et al., 1992; Lam and Bishop, 2007). This can explain the higher surface carbon export efficiency that we estimate SPF compared to NPF. Export efficiency has also been linked to bacterial productivity with efficient surface remineralisation limiting surface POC export, when most of the water column integrated bacterial productivity is restricted to the upper mixed layer (Dehairs et al.,

412 1992; Jacquet et al., 2011), which can be the case to varying degrees throughout the SO. In the STZ phytoplankton communities

413 are reported to be dominated by prokaryotic picoplankton including cyanobacteria and prochlorophytes (Mendes et al., 2015).

414 These groups utilise regenerated nutrients in the surface mixed layer tending towards diminished surface export efficiency

415 with high concentrations of non-sinking POC (Fan et al., 2020; Planchon et al. 2013). In addition to this, the potential influence

416 of high submesoscale activity, may explain the low mesopelagic Ba_{xs} measured at the STZ station of this study, despite it being

417 the station with the highest integrated PP (Figure S1). Linking temporally integrated remotely sensed PP to mesopelagic Ba_{xs}

418 stock, coupled with the added influence of physical dynamics affecting surface export efficiencies, along longer timescales,

419 could give better estimates of export and remineralisation signals throughout the SO, on an annual and basin scale. Our

420 estimates of percentage remineralised POC over remotely sensed PP may contribute to the improved modelling of the C cycle

421 over the SO, on an annual timescale.

5   Conclusions

423 Our unique early winter Ba_{xs} data were similar in magnitude and exhibited the same relationship with σ_θ and dissolved O_2

424 gradients as observed in summer, indicating that processes controlling this signal in summer are still driving the signal in early

425 winter. The expected decline of the mesopelagic Ba_{xs} signal to background values during winter was not observed in this study,

426 supporting the hypothesis that this remineralisation proxy likely has a longer timescale than previously reported. The absolute

427 decline might be delayed due to the cumulative behaviour of mesopelagic Ba_{xs}, ongoing remineralisation and barite

428 precipitation. The "true" SO background value may thus have to be measured at the very end of winter, prior to bloom initiation.

429 Significant positive correlations north and south of the PF, between mesopelagic Ba_{xs} stock and remotely sensed PP, integrated

430 from September to 1 month before sampling (Sept - T1), in combination with significant Ba_{xs} accumulation trends obtained

431 for the SO compilation dataset, suggest an annual timescale. They may also indicate that physical processes do not dominate

432 the mesopelagic signal on an annual scale, within the SO, and that biogeochemical factors are dominant. There is no significant

433 difference in mesopelagic Ba_{xs} and POC remineralisation, north and south of the PF, but the significantly higher integrated

434 remotely sensed PP to the north when compared to the south, indicates a greater export efficiency south of the PF. This is in

435 accordance with the phenomenon of HPLE regimes which are common throughout the SO, moreso north of the PF than south

436 of the PF (Fan et al., 2020). The longer timescale of Ba_{xs} and the cumulative behaviour of this proxy in the mesopelagic zone

437 make it possible to use Ba_{xs} on an annual scale for the estimation of POC remineralisation fluxes throughout the SO and to

438 better understand how variable environmental factors influence these processes on a basin scale. We believe that the

439 significance of these relationships will improve as more data become available (e.g., GEOTRACES IDP2021), which will

440 assist in better understanding and constraining the timescale of remineralisation and carbon export efficiency throughout the

441 SO.

6   Author contribution

This study was conceptualised by N.R.vH, H.P, G.S and E.B. Formal analysis, investigation and validation of data was carried out by N.R.vH, H.P, G.S, E.B and T.J.R-K. N.R.vH and T.J.R-K contributed towards the visualisation of the data. H.P, G.S, T.N.M, A.R, N.L. and E.B contributed towards supervision and resources. Funding was acquired by N.R.vH, T.N.M, A.R and E.B. All authors contributed towards writing, reviewing, and editing of the final manuscript.

7   Acknowledgments

8   Data availability

Data used in this study have been published in the online open-source repository Zenodo and can be accessed at https://doi.org/10.5281/zenodo.6583338 (van Horsten et al., 2022).

9   References

Anilkumar, N. and Sabu, P.: Physical process influencing the ecosystem of the indian sector of southern ocean-An overview, Proc. Indian Natl. Sci. Acad., 83(2), 363–376, doi:10.16943/ptinsa/2017/48960, 2017.

Ansorge, I. J., Jackson, J. M., Reid, K., Durgadoo, J. V, Swart, S. and Eberenz, S.: Evidence of a southward eddy corridor in the South-West Indian ocean, Deep. Res. Part II Top. Stud. Oceanogr., 119, 69–76, doi:10.1016/j.dsr2.2014.05.012, 2015.

Armstrong, R. A., Peterson, M. L., Lee, C. and Wakeham, S. G.: Settling velocity spectra and the ballast ratio hypothesis, Deep. Res. Part II Top. Stud. Oceanogr., 56(18), 1470–1478, doi:10.1016/j.dsr2.2008.11.032, 2009.

469 Barbur, V. A., Montgomery, D. C. and Peck, E. A.: Introduction to Linear Regression Analysis., Stat., 43(2), 339,
470   doi:10.2307/2348362, 1994.

471 Behrenfeld, M. J., Boss, E., Siegel, D. A. and Shea, D. M.: Carbon-based ocean productivity and phytoplankton physiology
472   from space, Global Biogeochem. Cycles, 19(1), 1–14, doi:10.1029/2004GB002299, 2005.

473 Bishop, J. K. B.: The barite-opal-organic carbon association in oceanic particulate matter, Nature, 332(6162), 341–343,
474   doi:10.1038/332341a0, 1988.

475 Bishop, J. K. B. and Edmond, J. M.: A new large volume filtration system for the sampling of oceanic particulate matter, J.
476   Mar. Res., 34, 181-198, 1976.

477 Bopp, L., Resplandy, L., Orr, J. C., Doney, S. C., Dunne, J. P., Gehlen, M., Halloran, P., Heinze, C., Ilyina, T., Séférian, R.,
478   Tjiputra, J. and Vichi, M.: Multiple stressors of ocean ecosystems in the 21st century: Projections with CMIP5 models,
479   Biogeosciences, 10(10), 6225–6245, doi:10.5194/bg-10-6225-2013, 2013.

480 Boyd, P. W., Claustre, H., Levy, M., Siegel, D. A. and Weber, T.: Multi-faceted particle pumps drive carbon sequestration in
481   the ocean, Nature, 568(7752), 327–335, doi:10.1038/s41586-019-1098-2, 2019.

482 Broecker, W. S., Takahashi, T. and Takahashi, T.: Sources and flow patterns of deep-ocean waters as deduced from potential
483   temperature, salinity, and initial phosphate concentration, J. Geophys. Res. Ocean., 90(C4), 6925–6939,
484   doi:10.1029/JC090iC04p06925, 1985.

485 Buesseler, K. O.: The decoupling of production and particulate export in the surface ocean, Global Biogeochem. Cycles, 12(2),
486   297–310, doi:10.1029/97GB03366, 1998.

487 Buesseler, K. O., Andrews, J. E., Pike, S. M., Charette, M. A., Goldson, L. E., Brzezinski, M. A. and Lance, V. P.: Particle
488   export during the Southern Ocean Iron Experiment (SOFeX), Limnol. Oceanogr., 50(1), 311–327,
489   doi:10.4319/lo.2005.50.1.0311, 2005.

490 Buesseler, K. O. and Boyd, P. W.: Shedding light on processes that control particle export and flux attenuation in the twilight
491   zone of the open ocean, Limnol. Oceanogr., 54(4), 1210–1232, doi:10.4319/lo.2009.54.4.1210, 2009.

492 Cardinal, D., Dehairs, F., Cattaldo, T. and André, L.: Geochemistry of suspended particles in the Subantarctic and Polar Frontal
493   zones south of Australia: Constraints on export and advection processes, J. Geophys. Res. Ocean., 106(C12), 31637–31656,
494   doi:10.1029/2000JC000251, 2001.

495 Cardinal, D., Savoye, N., Trull, T. W., André, L., Kopczynska, E. E. and Dehairs, F.: Variations of carbon remineralisation in
496   the Southern Ocean illustrated by the Baxs proxy, Deep. Res. Part I Oceanogr. Res. Pap., 52(2), 355–370,
497   doi:10.1016/j.dsr.2004.10.002, 2005.

498 Cavan, E. L., Le Moigne, F. A. C., Poulton, A. J., Tarling, G. A., Ward, P., Daniels, C. J., Fragoso, G. M. and Sanders, R. J.:
499   Attenuation of particulate organic carbon flux in the Scotia Sea, Southern Ocean, is controlled by zooplankton fecal pellets,
500   Geophys. Res. Lett., 42(3), 821–830, doi:10.1002/2014GL062744, 2015.

501   Cutter, G., Casciotti, K., Croot, P., Geibert, W., Heimbürger, L.-E., Lohan, M., Planquette, H. and van de Flierdt, T.: Sampling

502   and Sample-handling Protocols for GEOTRACES Cruises. Version 3, 139pp. & Appendices [online] Available from:

503   http://www.geotraces.org/images/stories/documents/intercalibration/Cookbook.pdf, 2017.

504   de Boyer Montégut, C., Madec, G., Fischer, A. S., Lazar, A. and Iudicone, D.: Mixed layer depth over the global ocean: An

505   examination of profile data and a profile-based climatology, J. Geophys. Res. C Ocean., 109(12), 1–20,

506   doi:10.1029/2004JC002378, 2004.

507   Dehairs, F., Baeyens, W. and Goeyens, L.: Accumulation of Suspended Barite at Mesopelagic Depths and Export Production

508   in the Southern Ocean, Science (80-.)., 258(5086), 1332–1335, doi:10.1126/SCIENCE.258.5086.1332, 1992.

509   Dehairs, F., Chesselet, R. and Jedwab, J.: Discrete suspended particles of barite and the barium cycle in the open ocean, Earth

510   Planet. Sci. Lett., 49(2), 528–550, doi:10.1016/0012-821X(80)90094-1, 1980.

511   Dehairs, F. and Goeyens, L.: Oxidation rate of organic carbon in the mesopelagic water column as traced by suspended barium-

512   barite, Integr. Mar. Syst. Anal., 205–217, 1996.

513   Dehairs, F., Goeyens, L., Stroobants, N., Bernard, P., Goyet, C., Poisson, A. and Chesselet, R.: On suspended barite and the

514   oxygen minimum in the Southern Ocean, Global Biogeochem. Cycles, 4(1), 85–102, doi:10.1029/GB004I001P00085,

515   1990.

516   Dehairs, F., Shopova, D., Ober, S., Veth, C. and Goeyens, L.: Particulate barium stocks and oxygen consumption in the

517   Southern Ocean mesopelagic water column during spring and early summer: Relationship with export production, Deep.

518   Res. Part II Top. Stud. Oceanogr., 44(1–2), 497–516, doi:10.1016/S0967-0645(96)00072-0, 1997.

519   Dehairs, F., Stroobants, N. and Goeyens, L.: Suspended barite as a tracer of biological activity in the Southern Ocean, Mar.

520   Chem., 35(1–4), 399–410, doi:10.1016/S0304-4203(09)90032-9, 1991.

521   de Jong, E., Vichi, M., Mehlmann, C. B., Eayrs, C., De Kock, W., Moldenhauer, M. and Audh, R. R.: Sea Ice conditions within

522   the Antarctic Marginal Ice Zone in winter 2017, onboard the SA Agulhas II., Univ. Cape Town, PANGAEA,

523   doi:https://doi.org/10.1594/PANGAEA.885211, 2018.

524   DeVries, T. and Weber, T.: The export and fate of organic matter in the ocean: New constraints from combining satellite and

525   oceanographic tracer observations, Global Biogeochem. Cycles, 31(3), 535–555, doi:10.1002/2016GB005551, 2017.

526   Ducklow, H. W., Steinberg, D. K. and Buesseler, K. O.: Upper ocean carbon export and the biological pump, Oceanography,

527   14(SPL.ISS. 4), 50–58, doi:10.5670/oceanog.2001.06, 2001.

528   Dymond, J., Suess, E. and Lyle, M.: Barium in Deep-Sea Sediment: A Geochemical Proxy for Paleoproductivity,

529   Paleoceanography, 7(2), 163–181, doi:10.1029/92PA00181, 1992.

530   Ehrhardt, M. (Manfred), Grasshoff, K., Kremling, K. (Klaus) and Almgren, T., Eds.: Methods of seawater analysis / edited by

531   K. Grasshoff, M. Ehrhardt, K. Kremling; with contributions by T. Almgren ... [et al.], Verlag Chemie, Weinheim., 1983.

532   Eriksen, R., Trull, T. W., Davies, D., Jansen, P., Davidson, A. T., Westwood, K. and Van Den Enden, R.: Seasonal succession

533   of phytoplankton community structure from autonomous sampling at the Australian Southern Ocean Time Series (SOTS)

534   observatory, Mar. Ecol. Prog. Ser., 589, 13–21, doi:10.3354/meps12420, 2018.

Fan, G., Han, Z., Ma, W., Chen, S., Chai, F., Mazloff, M. R., Pan, J. and Zhang, H.: Southern Ocean carbon export efficiency in relation to temperature and primary productivity, Sci. Rep., 10(1), 1–11, doi:10.1038/s41598-020-70417-z, 2020.

Ferrari, R. and Nikurashin, M.: Suppression of eddy diffusivity across jets in the Southern Ocean, J. Phys. Oceanogr., 40(7), 1501–1519, doi:10.1175/2010JPO4278.1, 2010.

Freeman, N. M., Lovenduski, N. S., Munro, D. R., Krumhardt, K. M., Lindsay, K., Long, M. C. and Maclennan, M.: The Variable and Changing Southern Ocean Silicate Front: Insights from the CESM Large Ensemble, Global Biogeochem. Cycles, 32(5), 752–768, doi:10.1029/2017GB005816, 2018.

Friedlingstein, P., Jones, M. W., O'Sullivan, M., Andrew, R. M., Hauck, J., Peters, G. P., Peters, W., Pongratz, J., Sitch, S., Le Quéré, C., Bakker, D. C. E., Canadell, J. G., Ciais, P., Jackson, R. B., Anthoni, P., Barbero, L., Bastos, A., Bastrikov, V., Becker, M., Bopp, L., Buitenhuis, E., Chandra, N., Chevallier, F., Chini, L. P., Currie, K. I., Feely, R. A., Gehlen, M., Gilfillan, D., Gkritzalis, T., Goll, D. S., Gruber, N., Gutekunst, S., Harris, I., Haverd, V., Houghton, R. A., Hurtt, G., Ilyina, T., Jain, A. K., Joetzjer, E., Kaplan, J. O., Kato, E., Klein Goldewijk, K., Korsbakken, J. I., Landschützer, P., Lauvset, S. K., Lefèvre, N., Lenton, A., Lienert, S., Lombardozzi, D., Marland, G., McGuire, P. C., Melton, J. R., Metzl, N., Munro, D. R., Nabel, J. E. M. S., Nakaoka, S.-I., Neill, C., Omar, A. M., Ono, T., Peregon, A., Pierrot, D., Poulter, B., Rehder, G., Resplandy, L., Robertson, E., Rödenbeck, C., Séférian, R., Schwinger, J., Smith, N., Tans, P. P., Tian, H., Tilbrook, B., Tubiello, F. N., van der Werf, G. R., Wiltshire, A. J. and Zaehle, S.: Global Carbon Budget 2019, Earth Syst. Sci. Data, 11(4), 1783–1838, doi:10.5194/essd-11-1783-2019, 2019.

Gall, M. P., Boyd, P. W., Hall, J., Safi, K. A. and Chang, H.: Phytoplankton processes. Part 1: Community structure during the Southern Ocean Iron RElease Experiment (SOIREE), Deep. Res. Part II Top. Stud. Oceanogr., 48(11–12), 2551–2570, doi:10.1016/S0967-0645(01)00008-X, 2001.

GEOTRACES Intermediate Data Product Group: The GEOTRACES Intermediate Data Product 2021 (IDP2021), NERC EDS British Oceanographic Data Centre NOC, doi: 10.5285/cf2d9ba9-d51d-3b7c-e053-8486abc0f5fd, 2021.

Gill, A. E.: Atmosphere-ocean dynamics, NEW YORK, U.S.A., ACADEMIC PRESS INC., 1982.

Gregor, L., Lebehot, A. D., Kok, S. and Scheel Monteiro, P. M.: A comparative assessment of the uncertainties of global surface ocean CO_2 estimates using a machine-learning ensemble (CSIR-ML6 version 2019a)-Have we hit the wall?, Geosci. Model Dev., 12(12), 5113–5136, doi:10.5194/gmd-12-5113-2019, 2019.

Gruber, N., Landschützer, P. and Lovenduski, N. S.: The variable southern ocean carbon sink, Ann. Rev. Mar. Sci., 11(September), 159–186, doi:10.1146/annurev-marine-121916-063407, 2019.

Honjo, S., Eglinton, T. I., Taylor, C. D., Ulmer, K. M., Sievert, S. M., Bracher, A., German, C. R., Edgcomb, V., Francois, R., Deboraiglesias-Rodriguez, M., Van Mooy, B. and Repeta, D. J.: Understanding the role of the biological pump in the global carbon cycle: An imperative for ocean science, Oceanography, 27(3), 10–16, doi:10.5670/oceanog.2014.78, 2014.

Ito, T., Follows, M. J. and Boyle, E. A.: Is AOU a good measure of respiration in the oceans?, Geophys. Res. Lett., 31(17), 1–4, doi:10.1029/2004GL020900, 2004.

568 Jacquet, S. H. M., Dehairs, F., Cardinal, D., Navez, J. and Delille, B.: Barium distribution across the Southern Ocean frontal
569   system in the Crozet-Kerguelen Basin, Mar. Chem., 95(3–4), 149–162, doi:10.1016/j.marchem.2004.09.002, 2005.

570 Jacquet, S. H. M., Dehairs, F., Dumont, I., Becquevort, S., Cavagna, A. J. and Cardinal, D.: Twilight zone organic carbon
571   remineralization in the Polar Front Zone and Subantarctic Zone south of Tasmania, Deep. Res. Part II Top. Stud. Oceanogr.,
572   58(21–22), 2222–2234, doi:10.1016/j.dsr2.2011.05.029, 2011.

573 Jacquet, S. H. M., Dehairs, F., Elskens, M., Savoye, N. and Cardinal, D.: Barium cycling along WOCE SR3 line in the Southern
574   Ocean, Mar. Chem., 106(1-2 SPEC. ISS.), 33–45, doi:10.1016/j.marchem.2006.06.007, 2007.

575 Jacquet, S. H. M., Dehairs, F., Lefèvre, D., Cavagna, A. J., Planchon, F., Christaki, U., Monin, L., André, L., Closset, I. and
576   Cardinal, D.: Early spring mesopelagic carbon remineralization and transfer efficiency in the naturally iron-fertilized
577   Kerguelen area, Biogeosciences, 12(6), 1713–1731, doi:10.5194/bg-12-1713-2015, 2015.

578 Jacquet, S. H. M., Dehairs, F., Savoye, N., Obernosterer, I., Christaki, U., Monnin, C. and Cardinal, D.: Mesopelagic organic
579   carbon remineralization in the Kerguelen Plateau region tracked by biogenic particulate Ba, Deep. Res. Part II Top. Stud.
580   Oceanogr., 55(5–7), 868–879, doi:10.1016/j.dsr2.2007.12.038, 2008a.

581 Jacquet, S. H. M., Savoye, N., Dehairs, F., Strass, V. H. and Cardinal, D.: Mesopelagic carbon remineralization during the
582   European Iron Fertilization Experiment, Global Biogeochem. Cycles, 22(1), 1–9, doi:10.1029/2006GB002902, 2008b.

583 Jochum, K. P., Nohl, U., Herwig, K., Lammel, E., Stoll, B. and Hofmann, A. W.: GeoReM: A new geochemical database for
584   reference materials and isotopic standards, Geostand. Geoanalytical Res., 29(3), 333–338, doi:10.1111/j.1751-
585   908x.2005.tb00904.x, 2005.

586 Kokoska, S. and Zwillinger, D.: CRC Standard Probability and Statistics Tables and Formulae, Student Edition., 2000.

587 Lam, P. J. and Bishop, J. K. B.: High biomass, low export regimes in the Southern Ocean, Deep. Res. Part II Top. Stud.
588   Oceanogr., 54(5–7), 601–638, doi:10.1016/j.dsr2.2007.01.013, 2007.

589 Laurenceau-Cornec, E. C., Trull, T. W., Davies, D. M., Bray, S. G., Doran, J., Planchon, F., Carlotti, F., Jouandet, M. P.,
590   Cavagna, A. J., Waite, A. M. and Blain, S.: The relative importance of phytoplankton aggregates and zooplankton fecal
591   pellets to carbon export: Insights from free-drifting sediment trap deployments in naturally iron-fertilised waters near the
592   Kerguelen Plateau, Biogeosciences, 12(4), 1007–1027, doi:10.5194/BG-12-1007-2015, 2015.

593 Le Moigne, F. A. C.: Pathways of Organic Carbon Downward Transport by the Oceanic Biological Carbon Pump, Front. Mar.
594   Sci., 6, doi:10.3389/fmars.2019.00634, 2019.

595 Legeleux, F. and Reyss, J. L.: 228Ra/226Ra activity ratio in oceanic settling particles: Implications regarding the use of barium
596   as a proxy for paleoproductivity reconstruction, Deep. Res. Part I Oceanogr. Res. Pap., 43(11–12), 1857–1863,
597   doi:10.1016/S0967-0637(96)00086-6, 1996.

598 Lemaitre, N., Planquette, H., Planchon, F., Sarthou, G., Jacquet, S., García-Ibáñez, M. I., Gourain, A., Cheize, M., Monin, L.,
599   André, L., Laha, P., Terryn, H. and Dehairs, F.: Particulate barium tracing of significant mesopelagic carbon
600   remineralisation in the North Atlantic, Biogeosciences, 15(8), 2289–2307, doi:10.5194/bg-15-2289-2018, 2018.

601 Maiti, K., Charette, M. A., Buesseler, K. O. and Kahru, M.: An inverse relationship between production and export efficiency
602   in the Southern Ocean, Geophys. Res. Lett., 40(8), 1557–1561, doi:10.1002/GRL.50219, 2013.

603 Marsay, C. M., Sanders, R. J., Henson, S. A., Pabortsava, K., Achterberg, E. P. and Lampitt, R. S.: Attenuation of sinking
604   particulate organic carbon flux through the mesopelagic ocean, Proc. Natl. Acad. Sci. U. S. A., 112(4), 1089–1094,
605   doi:10.1073/pnas.1415311112, 2015.

606 McDonnell, A. M. P. and Buesseler, K. O.: Variability in the average sinking velocity of marine particles, Limnol. Oceanogr.,
607   55(5), 2085–2096, doi:10.4319/LO.2010.55.5.2085, 2010.

608 Mendes, C. R. B., Kerr, R., Tavano, V. M., Cavalheiro, F. A., Garcia, C. A. E., Gauns Dessai, D. R. and Anilkumar, N.: Cross-
609   front phytoplankton pigments and chemotaxonomic groups in the Indian sector of the Southern Ocean, Deep. Res. Part II
610   Top. Stud. Oceanogr., 118, 221–232, doi:10.1016/j.dsr2.2015.01.003, 2015.

611 Morris, P. J., Sanders, R., Turnewitsch, R. and Thomalla, S.: 234Th-derived particulate organic carbon export from an island-
612   induced phytoplankton bloom in the Southern Ocean, Deep Sea Res. Part II Top. Stud. Oceanogr., 54(18–20), 2208–2232,
613   doi:10.1016/J.DSR2.2007.06.002, 2007.

614 Nissen, C., Vogt, M., Münnich, M., Gruber, N. and Haumann, F. A.: Factors controlling coccolithophore biogeography in the
615   Southern Ocean, Biogeosciences, 15(22), 6997–7024, doi:10.5194/bg-15-6997-2018, 2018.

616 Orsi, A. H., Whitworth, T. and Nowlin, W. D.: On the meridional extent and fronts of the Antarctic Circumpolar Current,
617   Deep. Res. Part I, 42(5), 641–673, doi:10.1016/0967-0637(95)00021-W, 1995.

618 Passow, U. and Carlson, C. A.: The biological pump in a high CO2 world, Mar. Ecol. Prog. Ser., 470(2), 249–271,
619   doi:10.3354/meps09985, 2012.

620 Petrou, K., Kranz, S. A., Trimborn, S., Hassler, C. S., Ameijeiras, S. B., Sackett, O., Ralph, P. J. and Davidson, A. T.: Southern
621   Ocean   phytoplankton   physiology   in   a   changing   climate,   J.   Plant   Physiol.,   203,   135–150,
622   doi:https://doi.org/10.1016/j.jplph.2016.05.004, 2016.

623 Planchon, F., Cavagna, A. J., Cardinal, D., André, L. and Dehairs, F.: Late summer particulate organic carbon export and
624   twilight zone remineralisation in the Atlantic sector of the Southern Ocean, Biogeosciences, 10(2), 803–820,
625   doi:10.5194/bg-10-803-2013, 2013.

626 Planquette, H. and Sherrell, R. M.: Sampling for particulate trace element determination using water sampling bottles:
627   Methodology   and   comparison   to   in   situ   pumps,   Limnol.   Oceanogr.   Methods,   10(5),   367–388,
628   doi:10.4319/lom.2012.10.367, 2012.

629 Pollard, R. T., Lucas, M. I. and Read, J. F.: Physical controls on biogeochemical zonation in the Southern Ocean, Deep. Res.
630   Part II Top. Stud. Oceanogr., 49(16), 3289–3305, doi:10.1016/S0967-0645(02)00084-X, 2002.

631 Pyle, K. M., Hendry, K. R., Sherrell, R. M., Legge, O., Hind, A. J., Bakker, D., Venables, H. and Meredith, M. P.: Oceanic
632   fronts control the distribution of dissolved barium in the Southern Ocean, Mar. Chem., 204(July), 95–106,
633   doi:10.1016/j.marchem.2018.07.002, 2018.

634   Rembauville, M., Briggs, N., Ardyna, M., Uitz, J., Catala, P., Penkerc'h, C., Poteau, A., Claustre, H. and Blain, S.: Plankton
635   Assemblage Estimated with BGC-Argo Floats in the Southern Ocean: Implications for Seasonal Successions and Particle
636   Export, J. Geophys. Res. Ocean., 122(10), 8278–8292, doi:10.1002/2017JC013067, 2017.

637   Riebesell, U.: Particle aggregation during a diatom bloom. II. Biological aspects, Mar. Ecol. Prog. Ser., 69(3), 281–291,
638   doi:10.3354/meps069281, 1991.

639   Rio, M. H., Guinehut, S. and Larnicol, G.: New CNES-CLS09 global mean dynamic topography computed from the
640   combination of GRACE data, altimetry, and in situ measurements, J. Geophys. Res. Ocean., 116(7), 1–25,
641   doi:10.1029/2010JC006505, 2011.

642   Robinson, C., Steinberg, D. K., Anderson, T. R., Arístegui, J., Carlson, C. A., Frost, J. R., Ghiglione, J. F., Hernández-León,
643   S., Jackson, G. A., Koppelmann, R., Quéguiner, B., Ragueneau, O., Rassoulzadegan, F., Robison, B. H., Tamburini, C.,
644   Tanaka, T., Wishner, K. F. and Zhang, J.: Mesopelagic zone ecology and biogeochemistry - A synthesis, Deep. Res. Part
645   II Top. Stud. Oceanogr., 57(16), 1504–1518, doi:10.1016/j.dsr2.2010.02.018, 2010.

646   Rosengard, S. Z., Lam, P. J., Balch, W. M., Auro, M. E., Pike, S., Drapeau, D. and Bowler, B.: Carbon export and transfer to
647   depth across the Southern Ocean Great Calcite Belt, Biogeosciences, 12(13), 3953–3971, doi:10.5194/bg-12-3953-2015,
648   2015.

649   Rutgers van der Loeff Michiel, M., Cai, P. H., Stimac, I., Bracher, A., Middag, R., Klunder, M. B. and van Heuven, S. M. A.
650   C.: 234Th in surface waters: Distribution of particle export flux across the Antarctic Circumpolar Current and in the
651   Weddell Sea during the GEOTRACES expedition ZERO and DRAKE, Deep. Res. Part II Top. Stud. Oceanogr., 58(25–
652   26), 2749–2766, doi:10.1016/j.dsr2.2011.02.004, 2011.

653   Ryan-Keogh, T. J., Thomalla, S. J., Mtshali, T. N., Van Horsten, N. R. and Little, H. J.: Seasonal development of iron limitation
654   in the sub-Antarctic zone, Biogeosciences, 15(14), 4647–4660, doi:10.5194/bg-15-4647-2018, 2018.

655   Sarmiento, J., & Gruber, N. Ocean Biogeochemical Dynamics, Princeton University Press, Princeton, Oxford
656   doi:10.2307/j.ctt3fgxqx, 2006.

657   Sathyendranath, S., Brewin, R. J. W., Brockmann, C., Brotas, V., Calton, B., Chuprin, A., Cipollini, P., Couto, A. B., Dingle,
658   J., Doerffer, R., Donlon, C., Dowell, M., Farman, A., Grant, M., Groom, S., Horseman, A., Jackson, T., Krasemann, H.,
659   Lavender, S., Martinez-Vicente, V., Mazeran, C., Mélin, F., Moore, T. S., Müller, D., Regner, P., Roy, S., Steele, C. J.,
660   Steinmetz, F., Swinton, J., Taberner, M., Thompson, A., Valente, A., Zühlke, M., Brando, V. E., Feng, H., Feldman, G.,
661   Franz, B. A., Frouin, R., Gould, R. W., Hooker, S. B., Kahru, M., Kratzer, S., Mitchell, B. G., Muller-Karger, F. E., Sosik,
662   H. M., Voss, K. J., Werdell, J. and Platt, T.: An ocean-colour time series for use in climate studies: The experience of the
663   ocean-colour climate change initiative (OC-CCI), Sensors (Switzerland), 19(19), doi:10.3390/s19194285, 2019.

664   Savoye, N., Trull, T. W., Jacquet, S. H. M., Navez, J. and Dehairs, F.: 234Th-based export fluxes during a natural iron
665   fertilization experiment in the Southern Ocean (KEOPS), Deep Sea Res. Part II Top. Stud. Oceanogr., 55(5–7), 841–855,
666   doi:10.1016/J.DSR2.2007.12.036, 2008.

667 Schlitzer, R.: Carbon export fluxes in the Southern Ocean: Results from inverse modeling and comparison with satellite-based
668　　estimates, Deep. Res. Part II Top. Stud. Oceanogr., 49(9–10), 1623–1644, doi:10.1016/S0967-0645(02)00004-8, 2002.

669 Shopova, D., Dehairs, F. and Baeyens, W.: A simple model of biogeochemical element distribution in the oceanic water
670　　column, J. Mar. Syst., 6(4), 331–344, doi:10.1016/0924-7963(94)00032-7, 1995.

671 Sigman, D. M., Hain, M. P. and Haug, G. H.: The polar ocean and glacial cycles in atmospheric CO_2 concentration, Nature,
672　　466(7302), 47–55, doi:10.1038/nature09149, 2010.

673 Sternberg, E., Jeandel, C., Robin, E. and Souhaut, M.: Seasonal cycle of suspended barite in the mediterranean sea, Geochim.
674　　Cosmochim. Acta, 72(16), 4020–4034, doi:10.1016/J.GCA.2008.05.043, 2008.

675 Sternberg, E., Tang, D., Ho, T. Y., Jeandel, C. and Morel, F. M. M.: Barium uptake and adsorption in diatoms, Geochim.
676　　Cosmochim. Acta, 69(11), 2745–2752, doi:10.1016/j.gca.2004.11.026, 2005.

677 Swart, S., Speich, S., Ansorge, I. J. and Lutjeharms, J. R. E.: An altimetry-based gravest empirical mode south of Africa: 1.
678　　Development and validation, J. Geophys. Res. Ocean., 115(3), 1–19, doi:10.1029/2009JC005299, 2010.

679 Takahashi, T., Sweeney, C., Hales, B., Chipman, D. W., Goddard, J. G., Newberger, T., Iannuzzi, R. A. and Sutherland, S. C.:
680　　The changing carbon cycle in the southern ocean, Oceanography, 25(3), 26–37, doi:10.5670/oceanog.2012.71, 2012.

681 Taylor, S. R. and McLennan, S. M.: The continental crust: Its composition and evolution, Blackwell Scientific Pub., Palo Alto,
682　　CA, United States. [online] Available from: https://www.osti.gov/biblio/6582885, 1985.

683 Thomalla, S. J., Fauchereau, N., Swart, S. and Monteiro, P. M. S.: Regional scale characteristics of the seasonal cycle of
684　　chlorophyll in the Southern Ocean, Biogeosciences, 8(10), 2849–2866, doi:10.5194/bg-8-2849-2011, 2011.

685 Trull, T. W., Passmore, A., Davies, D. M., Smit, T., Berry, K. and Tilbrook, B.: Distribution of planktonic biogenic carbonate
686　　organisms in the Southern Ocean south of Australia: A baseline for ocean acidification impact assessment, Biogeosciences,
687　　15(1), 31–49, doi:10.5194/bg-15-31-2018, 2018.

688 Twining, B. S., Nodder, S. D., King, A. L., Hutchins, D. A., LeCleir, G. R., DeBruyn, J. M., Maas, E. W., Vogt, S., Wilhelm,
689　　S. W. and Boyd, P. W.: Differential remineralization of major and trace elements in sinking diatoms, Limnol. Oceanogr.,
690　　59(3), 689–704, doi:https://doi.org/10.4319/lo.2014.59.3.0689, 2014.

691 van Beek, P., François, R., Conte, M., Reyss, J. L., Souhaut, M. and Charette, M.: 228Ra/226Ra and 226Ra/Ba ratios to track
692　　barite formation and transport in the water column, Geochim. Cosmochim. Acta, 71(1), 71–86,
693　　doi:10.1016/j.gca.2006.07.041, 2007.

694 Viljoen, J. J., Philibert, R., Van Horsten, N., Mtshali, T., Roychoudhury, A. N., Thomalla, S. and Fietz, S.: Phytoplankton
695　　response in growth, photophysiology and community structure to iron and light in the Polar Frontal Zone and Antarctic
696　　waters, Deep. Res. Part I Oceanogr. Res. Pap., 141(September), 118–129, doi:10.1016/j.dsr.2018.09.006, 2018.

697 Wright, S. W., van den Enden, R. L., Pearce, I., Davidson, A. T., Scott, F. J. and Westwood, K. J.: Phytoplankton community
698　　structure and stocks in the Southern Ocean (30-80°E) determined by CHEMTAX analysis of HPLC pigment signatures,
699　　Deep. Res. Part II Top. Stud. Oceanogr., 57(9–10), 758–778, doi:10.1016/j.dsr2.2009.06.015, 2010.

700 Zhuang, J.: xESMF: Universal Regridder for GeospatialData, https://github.com/JiaweiZhuang/xESMF, 2018.